

Article

Optimizing Structural Patterns for 3D Electrodes in Lithium-Ion Batteries for Enhanced Fast-Charging Capability and Reduced Lithium Plating

Yannic Sterzl *  and Wilhelm Pfleging * 

Institute for Applied Materials—Applied Materials Physics (IAM-AWP), Karlsruhe Institute of Technology, 76344 Eggenstein-Leopoldshafen, Germany

* Correspondence: yannic.sterzl@kit.edu (Y.S.); wilhelm.pfleging@kit.edu (W.P.)

Abstract: The most common pattern types for anode structuring, in particular the line, grid, and hexagonal-arranged hole pattern were evaluated in a comparable setup in full-cells and symmetrical cells. The cells with structured electrodes were compared to reference cells with unstructured anodes of similar areal capacity (4.3 mAh cm^{-2}) and the onset of lithium plating during fast-charging was determined in situ by differential voltage analysis of the voltage relaxation and ex situ by post-mortem analysis. Furthermore, electrochemical impedance spectroscopy measurements on symmetrical cells were used to determine the ionic resistance of structured and unstructured electrodes of similar areal capacity. All cells with structured electrodes showed lower ionic resistances and an onset of lithium plating shifted to higher C-rates compared to cells with unstructured electrodes. The structure patterns with capillary structures, i.e., lines and grids, showed significant reduced lithium plating during fast-charging and a higher rate capability compared to reference cells with unstructured electrodes and cells with hole structured electrodes. The continuous rewetting of the electrode with liquid electrolyte by capillary forces and the reduced ionic resistance of the 3D electrode are identified as key factors in improving overall battery performance. The data of the studied cells were used to calculate the resulting energy and power densities of prospective commercial pouch cells and potential pitfalls in the comparison to cells with unstructured electrodes were identified.



Citation: Sterzl, Y.; Pfleging, W.

Optimizing Structural Patterns for 3D Electrodes in Lithium-Ion Batteries for Enhanced Fast-Charging Capability and Reduced Lithium Plating.

Batteries **2024**, *10*, 160. <https://doi.org/10.3390/batteries10050160>

Academic Editor: Stefan Adams

Received: 17 April 2024

Revised: 3 May 2024

Accepted: 7 May 2024

Published: 11 May 2024



Copyright: © 2024 by the authors. Licensee MDPI, Basel, Switzerland. This article is an open access article distributed under the terms and conditions of the Creative Commons Attribution (CC BY) license (<https://creativecommons.org/licenses/by/4.0/>).

1. Introduction

The increasing electrification, especially in the transport sector, requires electrochemical energy storage systems with high energy and power density, long lifetime, and high safety standards [1]. For electric vehicles to gain wider acceptance over conventional combustion engine-powered vehicles, it is crucial to address the advantages that conventional vehicles still hold in terms of refueling and range [1,2]. The development of active materials for lithium-ion batteries with high specific capacities, such as silicon on the anode side and nickel-rich nickel-manganese-cobalt oxides (NMC) on the cathode side, as well as improvements in electrode design, like the implementation of thick-film electrodes, i.e., electrode thickness $> 100 \mu\text{m}$ and areal capacity $> 4 \text{ mAh cm}^{-2}$, referred to single-side coated electrodes, are leading to the high specific and volumetric energy densities of today's automotive battery cells of up to 300 Wh kg^{-1} and 650 Wh L^{-1} [1,3–7]. With a specific energy density of up to 300 Wh kg^{-1} in combination with a total energy of 30–100 kWh of state-of-the-art automotive battery packs, driving ranges of larger than 500 km are already possible [1,3]. Greater difficulties are associated with the fast-charging requirements for automotive cells. A charging time of less than 15 min to a state of charge (SoC) of about 80%, which corresponds to a current rate (C-rate) of 3.2C–4C, is considered the target to

reach in order to close the gap in time needed to refill compared to combustion engine-powered vehicles [2]. For high-energy cells with thick-film electrodes, in addition to the fast-charging limitation of the used active material in terms of charge transfer resistance and solid-state diffusion, the depletion of lithium-ions in the electrolyte during fast-charging on the anode side is considered a bottleneck [2,7–9]. Furthermore, the resulting concentration overpotential within the electrode during fast-charging, namely in the active material and in the electrolyte, can lead to a potential below 0 V vs. Li/Li⁺ in parts of the anode, and lithium plating becomes thermodynamically favorable [10]. Lithium plating is considered a serious safety risk, as growing lithium dendrites can cause an internal short circuit in the cell leading to a thermal runaway, and should therefore be avoided [11]. In addition to the safety risks associated with lithium plating, there is also a significant decrease in capacity related to it. The continuous growth of the solid electrolyte interphase (SEI) on freshly plated lithium as well as the formation of electronically isolated and electrochemically inactive lithium, due to the combination of the processes of lithium plating and lithium stripping, lead to irreversible loss of lithium inventory [12–14]. Various approaches are being investigated to enhance the fast-charging capability of high-energy cells. On the material level, implementing active materials with high-rate capability, like hard carbons is the subject of current research [15–17]. On the electrode level, the controlled adjustment of electrode parameters like porosity, particle size distribution, as well as the implementation of an active material gradient by multilayer coating are studied [18–21]. A further possibility at electrode level is the reduction in the effective tortuosity by electrode structuring, either by laser ablation, mechanical embossing, 3D printing, or freeze casting [22–26]. The laser-assisted patterning of electrodes has the advantage that it can be integrated into manufacturers' existing production lines and no new cell chemistry needs to be implemented to improve fast-charging capability [27]. However, to integrate the process into industrial cell production, the laser structuring process must keep pace with the belt speed in production. The upscaling of the structuring process is therefore the current subject of research, and the concept was recently transferred to large-format pouch cells demonstrating a technology readiness level (TRL) of 5 to 6 [28,29]. Several pattern types have been investigated and used in research and development, including a hexagonal arrangement of holes, parallel oriented lines, and grid patterns or combinations and variations of the above [30–39].

Chen et al. [31] realized a hexagonal-arranged hole pattern with a structure pitch of 85 μm in graphite electrodes. The electrodes with an initial areal capacity of 3.2 mAh cm⁻² were ablated using nanosecond laser pulses operating at a wavelength of 355 nm and resulted in structured electrodes with an areal capacity of 2.9 mAh cm⁻². 2.2 Ah pouch cells with structured and unstructured graphite anodes and unstructured NMC532 cathodes were studied regarding their fast-charging capability at 4C and 6C. The capacity retention for pouch cells with structured anodes after 100 cycles of fast-charging at 6C and 4C remained at 93% and 97%, respectively, compared to 59% and 69% for the cells with unstructured anodes with an areal capacity of 3.2 mAh cm⁻². In addition, new reference cells with adjusted loading and porosity were manufactured to compensate for the influence of mass loss due to the structuring. These cells also showed a lower fast-charging capacity compared to the cells with structured electrodes of the same loading and porosity. The authors detected by post-mortem scanning electron microscopy (SEM), the deposition of lithium due to plating on large areas on the surface of the reference electrodes, and only a minor amount of lithium due to plating was observed on the surface of the structured electrodes. The suppressed lithium plating on structured electrodes was attributed to a more homogeneous reaction rate in structured electrodes compared to the unstructured ones derived from simulation-based results.

Zheng et al. [37] demonstrated a lower capacity fading and higher fast-charging capability of structured graphite and silicon/graphite electrodes with line and grid patterns. The half-cells with structured electrodes, with a thickness of 75 μm for graphite and 55 μm for silicon/graphite, exceeded the cells with unstructured reference electrodes in terms of the charging capacities achieved at C-rates greater than C/2. In laser-structured electrodes, the volume expansion of silicon and graphite resulted in a significant reduction in mechanical degradation, as shown by post-mortem analyses.

So far, the impact of the pattern-types of laser structured anodes in full-cells on the fast-charging capability and the lithium plating have not been investigated. In the study presented, the fast-charging capability and lithium plating behavior of full-cells with hole, line and grid structured anodes were investigated and qualified in a comparable setup for the first time. Furthermore, the structured electrodes were examined regarding their ionic resistance in symmetrical cells. Particular attention was paid to the mass loss due to laser ablation and the resulting cell balancing of the cells with structured and unstructured electrodes. The targeted mass loss due to structuring in this work was 10% and was thus based on comparable values in the literature [31]. The mass loss of the structured electrodes has been adjusted to a similar level by adjusting the structure pitch to the respective structure type. For a comparison of cells with structured and unstructured electrodes, it is crucial that the loadings of the electrode are kept the same. For that, the mass loss due to structuring was compensated in electrode manufacturing by thicker electrode coatings. Otherwise, the cell balancing would be changed or, in the case of structuring the cathode, the capacity would be reduced.

2. Materials and Methods

2.1. Electrode Preparation

Artificial graphite (Gr, SPGPT808, Targray Inc., Kirkland, QC, Canada) and carbon black (CB, Timcal Super C65, MTI Corporation, Richmond, CA, USA) were mixed with a water-based 2 wt.% sodium carboxymethyl cellulose solution (CMC, MTI Corporation, Richmond, CA, USA) with a centrifugal mixer (Speedmixer DAC 150 SP, Hauschild, Hamm, Germany). Once a homogeneous mixture of the slurry was achieved, a styrene butadiene rubber solution (SBR, 50 wt.% solid content, MTI Corporation, Richmond, CA, USA) was added and stirred into the slurry with a centrifugal mixer at low rotational speed (60 s at 1000 rpm). The composition of the anode slurry is summarized in Table 1. The anode slurry with a solid content of 51.2 wt.% was doctor-blade coated onto 9 μm thick copper foil and dried at room temperature. Subsequently, the anodes were calendered to a porosity of 40%. To realize structured and unstructured graphite electrodes of similar areal capacity, two electrodes with an areal capacity of 4.3 mAh cm^{-2} and 5.0 mAh cm^{-2} were prepared to balance the loss of active material due to the laser ablation. For the cathode, polycrystalline lithium-nickel-manganese-oxide (NMC 622, BASF SE, Ludwigshafen, Germany), carbon black (C-NERGY Super C65, Imerys G & C Belgium, Willebroek, Belgium), and conductive graphite (KS6L, Imerys G&C Switzerland Ltd., Bodio, Switzerland) were mixed with a N-methyl-2-pyrrolidone (NMP, Merck KGaA, Darmstadt, Germany) based polyvinylidene fluoride (PVDF, Solef[®] 5130, Solvay Specialty Polymers, Brussel, Belgium) solution with a weight proportion of 1:10 using a centrifugal mixer. Subsequently, the cathode slurry with an adjusted solid content of 66.7 wt.% was doctor-blade coated onto 20 μm thick aluminium foil and dried for 3 h at 90 °C. Subsequently, the cathodes were calendered to a porosity of 35%. The composition of the cathode slurry is summarized in Table 1. The porosity values for anode and cathode were calculated according to the common procedure described in Equation (S2) [38].

Table 1. Composition of electrode slurries (Anode composition adapted from [40]).

Material	Anode Mass Fraction/wt.%	Cathode Mass Fraction/wt.%
graphite	93	-
CB	1.4	3
CMC	1.87	-
SBR	3.73	-
NMC622	-	92
PVDF	-	3
conductive graphite	-	2
solid content/wt.%	51.2	66.7

2.2. Laser Structuring

Laser ablation was performed on the calendered graphite anodes using a laser source (FX600-2-GFH, EdgeWave GmbH, Würselen, Germany) with a maximum average laser power of 300 W, a pulse length of 600 fs, and an operating wavelength of 1030 nm. The laser source is implemented in a laser material processing system (MSV203 Laser Patterning Tool, M-SOLV LTD, Oxford, UK) which is capable of roll-to-roll (R2R) processing. The calculated beam waist radii are 11.95 μm and 10.85 μm due to the slightly elliptical output beam profile and differences of beam quality factor (M^2) in x- and y-direction. The hexagonal-arranged hole pattern was structured at a scanning velocity of 13.5 m s^{-1} , a repetition rate of 100 kHz, and a pulse energy of 70 μJ . The grid and line pattern were structured at a scanning velocity of 2 m s^{-1} and 20 m s^{-1} , a repetition rate of 150 kHz and 1.5 MHz, and a pulse energy of 33.3 μJ . All pattern types were structured with an adjusted number of laser beam passes until the current collector has been exposed, varying from 32 to 57 passes. The differences in the process parameters are due to the varying complexity of the geometries. The laser structured anodes were examined by SEM (Philips FEI XL 30S, FEI Technology Inc., Hillsboro, OR, USA) regarding debris formation as well as mechanically and thermally driven material modification.

2.3. Cell Assembly and Electrochemical Testing

Anodes and cathodes with a diameter of 15 mm and 12 mm, respectively, were laser cut and subsequently dried in a vacuum oven at 100 °C for 24 h to remove excess moisture. Full-cells and symmetrical cells in CR2032 coin cell format were assembled in an argon-filled glove box (LAB master pro sp, M. Braun Intergas-Systeme GmbH, Garching, Germany) with $\text{H}_2\text{O} < 0.1 \text{ ppm}$ and $\text{O}_2 < 0.1 \text{ ppm}$. As electrolyte, 1.3 M LiPF₆ in a mixture of ethylene carbonate and ethyl methyl carbonate (EC/EMC 3:7) with 5 wt.% FEC additive was used. Each full-cell was constructed of one anode and cathode, 160 μL of electrolyte, and a 25 μm polypropylene (PP) separator. In the case of symmetrical cells, two anodes with a diameter of 15 mm, 160 μL electrolyte, and a PP separator were utilized. For the calculation of the area specific resistance, the footprint (176.7 mm^2) of the electrodes was applied. For all investigated anode structure pattern, at least 3 full- and symmetrical cells were built. To ensure a homogeneous wetting of the electrodes and separator with liquid electrolyte, full-cells were stored for 20 h and symmetrical cells for 24 h at 20 °C prior to further electrochemical analyses. Galvanostatic characterization was performed using a battery cycler (BT 2000, Arbin Instruments, College Station, TX, USA). The formation of the full-cells was performed in a voltage window of 3.0–4.2 V following a constant current (CC) constant voltage (CV) protocol at a charging and discharging current rate (C-rate) of 0.05C and a cut-off current in the charging CV phase of 0.02C. The initial capacity of the cells was calculated with a practical specific capacity of 172 mAh g⁻¹ for NMC 622 and 330 mAh g⁻¹ for graphite. Between each charging and discharging step there was a rest period of 15 min. The C-rate for the rate capability analysis was calculated on base of the discharge capacity of the cells in the third formation cycle. Electrochemical impedance spectroscopy (EIS) on symmetrical cells were measured using a battery cycler (BCS810, Biologic, Seyssinet-Pariset, France) between 10 mHz and 10 kHz with a voltage amplitude of 10 mV. The rate capability

analyses consisted of a CCCV charging protocol with increasing charging rates from 0.1C to 5C shown in Table 2. In the first four cycles at each C-rate, there was a 15 min rest period after each charging and discharging cycle. For the fifth cycle at each C-rate, the CV phase was not only limited by a cut-off current but also limited by time (15 min). Furthermore, for this cycle, the rest period after charging and discharging was extended to 4 h to study the voltage relaxation of the cells.

Table 2. CCCV protocol of the rate capability analyses.

	0.1C	0.2C	0.5C	1C	2C	3C	5C
Charging CC	0.1C	0.2C	0.5C	1C	2C	3C	5C
Cut-off CV	0.05C	0.1C	0.1C	0.1C	0.1C	0.1C	0.1C
Discharge CC	0.1C	0.2C	0.2C	0.2C	0.2C	0.2C	0.2C
Repetitions	5	5	5	5	5	5	5

2.4. Post-Mortem Analysis

Discharged cells, at a voltage of 3 V, were disassembled in an argon filled glovebox. The electrodes were separated and stored in dimethyl carbonate (DMC) for a total time of 1 h. Subsequently, the electrodes were rinsed with DMC and dried in the glovebox. To study the cell degradation, the electrodes were transferred under ambient conditions to an optical microscope (VHX7000, KEYENCE, Osaka, Japan) and subsequently to the SEM.

3. Results and Discussion

3.1. Electrode Characterization

Figure 1a–f shows the top-view SEM images of the laser patterned electrodes. For all three investigated structure patterns, no debris on the electrode surface have been found. Nevertheless, a modification of the active material induced by the laser structuring, as described in the literature for graphite anodes, cannot be completely ruled out [33]. Since the mass loss due to structuring is a function of the pattern type, pitch (p_s), and structure dimension (w), the individual structuring parameters had to be adjusted separately for each pattern type. As shown in Figure 1a–c, the chosen p_s varied from 580 μm for the grid pattern to 300 μm for the line pattern and 135 μm for the hole pattern, and the resulting mass loss of each electrode type, determined by weighting the electrodes before and after structuring, is listed in Table 3. The average mass loss over all structures is 11.0% with the highest mass loss of 12.4% for the electrodes structured with the line pattern and the lowest mass loss of 9.7% for the electrodes structured with the hole pattern. The measured average w of each structure from the higher magnification SEM images in Figure 1d–f are 46.3 μm , 38.7 μm , and 33.7 μm for the hole, line, and grid pattern, respectively. Assuming the shape of the holes as cylinders and the shape of the line structures of the line and grid pattern as cuboids, the calculated mass loss is 10.7%, 12.9%, and 11.3% for the hole, line, and grid pattern and with that in good agreement to the measured mass loss. The slightly higher calculated mass loss compared to the measured mass loss can be explained by slightly tapered structures towards the bottom of the electrode, which is often described in the literature and depends on the laser ablation characteristics [41,42]. The resulting areal capacities of the electrodes have a maximum deviation of 4.4% in case of the hole structured electrodes to the unstructured reference electrode. With that, the comparability of all investigated cells is given by similar N/P-ratios in the range of 1.14–1.17 and cell capacities in the range of 4.07 mAh to 4.18 mAh (Table 3).

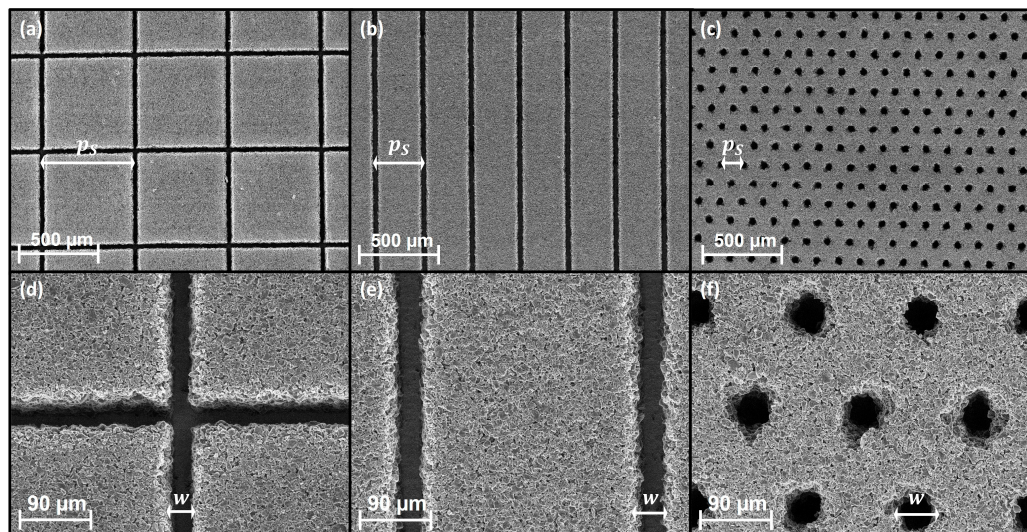


Figure 1. Top-view SEM images of the laser structured anodes with grid (a,d) line (b,e) and hole (c,f) pattern with indicated structure dimension (w) and pitch (p_S). (SEM: 10 kV accelerating voltage).

Table 3. Specification of the tested full-cells after formation. Each pattern type consists of a set of three cells.

	Unstructured	Hole	Line	Grid
Areal capacity anode/mAh cm ⁻²	4.33 ± 0.01	4.52 ± 0.04	4.38 ± 0.01	4.45 ± 0.01
Cell capacity/mAh	4.13 ± 0.04	4.18 ± 0.05	4.07 ± 0.03	4.09 ± 0.01
N/P-ratio	1.14 ± 0.00	1.17 ± 0.00	1.16 ± 0.00	1.17 ± 0.00
ICE/%	85.75 ± 1.75	83.48 ± 4.56	86.39 ± 0.23	86.37 ± 0.19
Mass loss (anode)/%	-	9.7 ± 0.6	12.4 ± 0.1	11.0 ± 0.2

In addition to the characterization of the influence of structured anodes on the electrochemical performance in full-cells, symmetrical cells with structured and unstructured electrodes were built. The anodes used in the symmetrical cells are similar to the set of anodes utilized in the full-cells. Symmetrical cells in blocking conditions, so faradaic processes are suppressed, are used to evaluate porous electrodes regarding their ionic resistivity [43,44]. To realize blocking conditions, a so-called non-intercalating electrolyte can be utilized, or in the case of an intercalating electrolyte, electrodes in a SOC in which faradaic reactions are suppressed can be used [44]. For anodes, this refers to a fully lithiated or delithiated state [44]. The results of the EIS measurements were fitted to the equivalent circuit shown in Figure 2c consisting of a resistor and a generalized finite Warburg element (Equation (S19)). The generalized finite Warburg element is mathematically identical to a transmission line model of resistors and constant phase elements typically used to describe porous electrodes [45]. The pure resistance represents the sum of all ohmic resistances in the cell as electrolyte and electrical resistance. No semicircles in the high and low frequency regime were observed in the Nyquist plot of our measurements (Figure 2a). A semicircle in the high frequency region of the Nyquist plot would be expected for a high contact resistance or faradaic processes, but can also be observed in the case of various pore geometries [46,47]. The highest ionic resistance of $30.0 \pm 2.2 \Omega \text{ cm}^2$ was measured for the unstructured reference electrode. All investigated structure patterns showed lower ionic resistances compared to the unstructured reference electrode, with $21.0 \pm 0.8 \Omega \text{ cm}^2$ for the hole structure, $21.8 \pm 1.3 \Omega \text{ cm}^2$ for the line structure, and $23.7 \pm 0.2 \Omega \text{ cm}^2$ for the grid structure (Figure 2b). A reduction in ionic resistance of structured electrodes compared to unstructured electrodes with unmatched areal capacity due to mass loss during structuring is known in the literature [35]. Due to the increase in ionic resistance with increasing coating thickness, such a comparison puts the unstructured electrodes at a disadvantage [44]. Our

results reveal that structured electrodes of various structure patterns also exhibit lower ionic resistances compared to reference electrodes with similar areal capacity and with that a decreased layer thickness compared to structured electrodes.

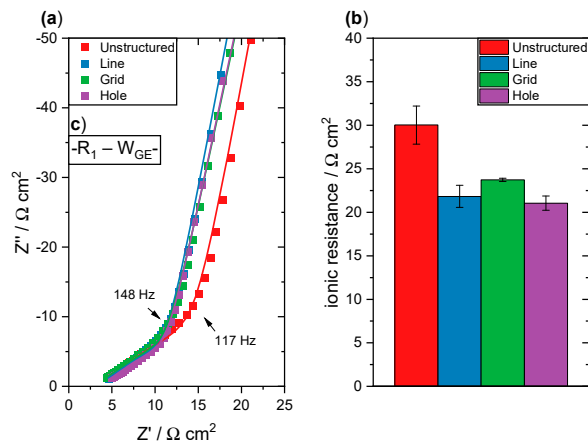


Figure 2. (a) Nyquist plot of EIS data (squares) and related fits (solid lines) on symmetrical cells with structured and unstructured electrodes; (b) the measured ionic resistance; and (c) the used equivalent circuit with R_1 as resistor and W_{GE} as generalized finite Warburg element.

3.2. Fast-Charging Capability

Figure 3 shows the specific charge capacity after the CC (Figure 3a) and CCCV phase (Figure 3b) without the 5th cycle at each C-rate, since the CCCV phase was additionally limited in time instead of a pure current limitation for this cycle. A gradual decline in specific capacity can be observed during cycling at 0.1C and 0.2C until the specific capacity stabilizes in the cycles at 0.5C for cells with electrodes of all structure types and the unstructured reference electrode. All cells show a decrease in achievable CC specific capacity with an increasing C-rate, with a significant drop in capacity between 1C and 2C (Figure 3a). The loss in achievable specific capacity between 1C and 2C is most pronounced for cells with unstructured electrodes, with a decrease from 109 mAh g^{-1} at 1C to 53 mAh g^{-1} at 2C. The highest specific capacity at C-rates greater than 0.5C was reached by cells with line structured electrodes, with 95 mAh g^{-1} at 2C and 63 mAh g^{-1} at 3C. While cells with grid structured electrodes showed similar results compared to the cells with line structured electrodes (89 mAh g^{-1} at 2C and 53 mAh g^{-1} at 3C), the cells with hole structured electrodes showed a lower fast-charging capability, reflected in lower reached specific capacities compared to the cells with electrodes of other structure types at C-rates greater than 1C. The obtained specific capacity of 72 mAh g^{-1} at 2C and 33 mAh g^{-1} at 3C of the cells with hole structured electrodes are in the range between the cells with unstructured electrodes and line as well as grid structured electrodes. The higher fast-charging capability of cells with structured electrodes can be assigned to an improved lithium-ion diffusion kinetic in the structured electrodes [48]. This is consistent with the results of the experiments on symmetrical cells, where the cells with structured electrodes had a lower ionic resistance compared to cells with unstructured electrodes (Figure 2b). The lower performance in fast-charging of the cells with hole structured electrodes compared to cells with electrodes of the other structure types, on the other hand, is contrary to the results on symmetrical cells, where the cells with structured electrodes of all pattern types had similar ionic resistances. However, the larger standard deviations in the set of cells with hole structured electrodes and unstructured electrodes compared to cells with line and grid structured electrodes are also noteworthy and are an indication of enhanced electrolyte wetting and rewetting promoted by the capillary structures present in the electrode with line and grid structures [49,50]. While the reached specific capacity in the CC phase is an indication for the fast-charging capability, the reached specific capacity in the CCCV phase gives information about the cell's capacity fade. To quantify the capacity retention,

five checkup cycles at 0.2C were appended to the rate capability analysis. As can be seen in Figure 3b, the reached specific capacity after CCCV charging decreases irreversibly starting at C-rates greater than 1C for cells with unstructured electrodes. This drop in capacity can be attributed to lithium plating starting for charging at C-rates higher than 1C for the cells with unstructured electrodes (see voltage relaxation analysis and post-mortem analysis presented below). The cells with structured electrodes showed a more stable cycling behavior with a capacity retention of 89%, 86%, and 84% for the cells with line, grid, and hole structured electrodes compared to the cells with unstructured electrodes with a capacity retention of 65%.

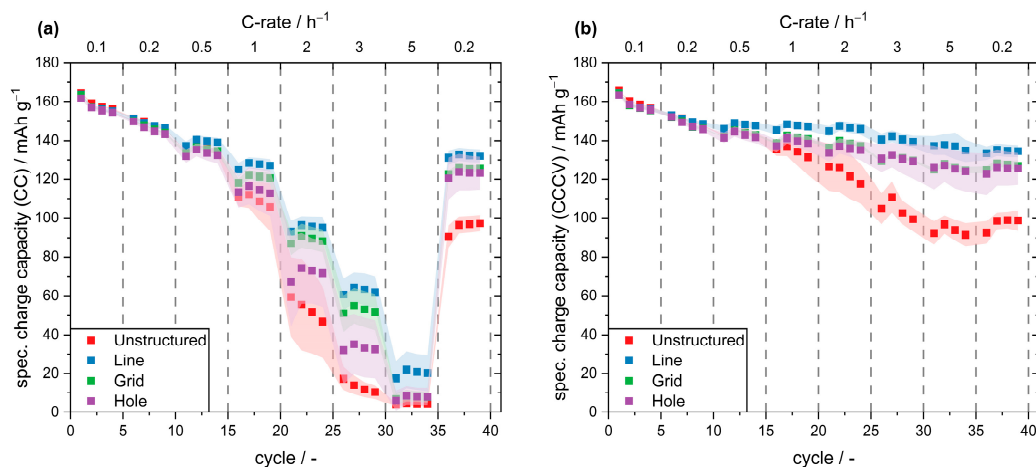


Figure 3. Specific charge capacity after the CC (a) and CCCV (b) phase (without the fifth cycle at each C-rate). The shading indicates the extent of the standard deviation.

The respective SOC achieved during the fifth cycle at each C-rate, with the CCCV phase additionally limited in time (15 min), is shown in Figure 4a. A time limitation of the CV phase is necessary for the subsequent analysis of the voltage relaxation, but also more accurately represents fast-charging applications than a current limit. An SOC of 80% is often considered as target in the literature regarding fast-charging and is indicated by the dotted line in Figure 4a. For cells with structured electrodes, an SOC of 80% can be reached after charging at 2C, while cells with unstructured reference electrodes can only be charged at 1C to reach the same SOC. Of all the structure patterns investigated, only the cells with line structured electrodes were able to be charged to an SOC of 80% at 3C. Due to the CV phase, the charging time up to an SOC of 80% does not correlate directly with the C-rate. The proportion of the SOC achieved after the CC and the CV phase is indicated by the different shades of the columns in Figure 4a. The positive impact of the structuring with regard to an enhanced diffusion kinetics and thus, the fast-charging capacity is not only evident in the CCCV phase, but also in the CC phase. The SOC achieved in the CC phase is higher for cells with structured electrodes charged at C-rates greater than 1C compared to the reference cells. While at 2C the majority of the gained SOC is charged in the CC phase, from 3C, the CV phase accounts for the largest share on the reached SOC. At 5C, the CC phase only accounts for a maximum of 18% (cells with line structured electrodes) of the SOC reached. This also affects the charging times to a SOC of 80% (Figure 4b). While the charging times halve from 0.5C to 1C, this is no longer the case from 1C to 2C, as the proportion of the SOC achieved in the CV phase increases. This is particularly evident for cells with line structured electrodes between 2C and 3C. It is worth noting that only cells with line-structured electrodes between 2C and 3C reached 80% SOC in the 5th cycle. However, in this case, the charging time required to reach an SOC of 80% is only reduced by 2.45 min, which means that charging at higher C rates than 2C does not offer significantly more advantages regarding fast-charging capability in the case of cells with thick electrodes with high areal capacity >4 mAh cm⁻². If the areal capacity of the electrodes and thus

also the coating thickness is reduced, the proportion of achieved capacity in the CC-phase increases at C-rates > 2C, which enables a further reduction in the possible charging time to a SOC of 80% [51].

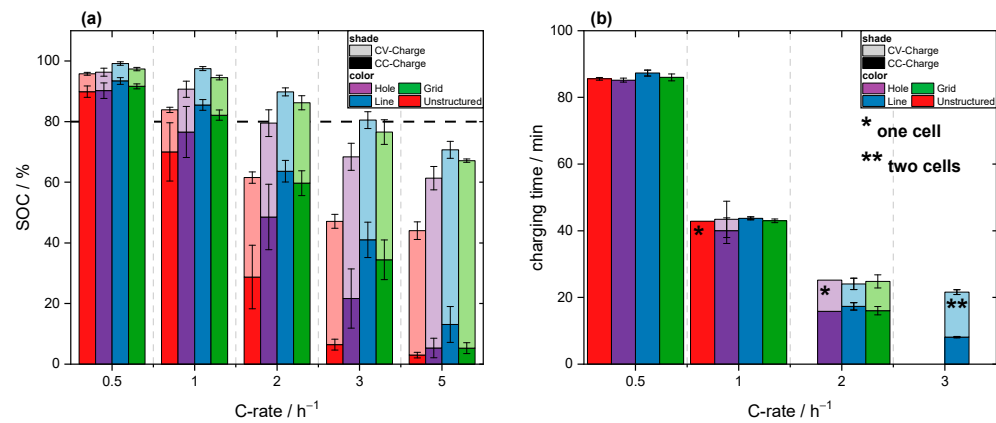


Figure 4. SOC after CCCV charging (a) and the required charging time to a SOC of 80% (b) as a function of C-rate (fifth cycle of the respective C-rate shown; the star symbols indicate the number of cells—out of 3 cells—that have fulfilled the criterion).

3.3. Voltage Relaxation Analyses

To gain a profound insight into the higher capacity retention of cells with structured electrodes, the voltage relaxation after every fifth cycle at each C-rate was measured for a duration of 4 h. The onset of lithium plating can be determined from the voltage relaxation after fast-charging [10,14,32]. During the rest period after charging, the plated lithium re-intercalates into the active material, affecting the concentration relaxation in the active material. This results in a characteristic plateau in the transient voltage [10]. The plateau in the transient voltage in the rest period appears as a peak in the differential voltage analysis (dV/dt). The corresponding peak width as well as the peak position can indicate the amount of plated lithium [52]. In Figure 5, the dV/dt (solid line) and the voltage (dashed line) are plotted as a function of time for representative cells with unstructured and structured electrodes (dV/dt plots of all investigated cells can be found in Figure S1). The reference cells showed lithium plating at C-rates between 1C and 3C as indicated by a peak in the dV/dt, which is also the C-rate range of excessive capacity fading observed in the rate capability test (Figure 3b). Noteworthy is the missing peak in the dV/dt at 5C for the reference cells as one would expect plating at the highest studied C-rate. The missing peak in the dV/dt matches the result of the rate capability analysis, in which the reached CCCV capacity also appears to stabilize at 5C for the reference cells and can be explained with a decreasing lithium inventory with ongoing plating. The decreasing lithium inventory changes the capacity balance of the anode and the cathode in a way that the electrode potential on the anode remains above 0 V vs. Li/Li⁺ and plating is not thermodynamic favorable [13]. In contrast to the unstructured reference cells, the onset of lithium plating, as indicated by a peak in the dV/dt analysis, is shifted to higher C-rates for cells with structured electrodes. Cells with electrodes of all studied structure types showed a peak in the dV/dt after charging at 3C and 5C. For the grid and hole structures, a less pronounced saddle point is noticeable in the dV/dt after charging at 2C, which is consistent to the lower capacity retention observed for cells with electrodes of these two pattern types compared to the cells with line structured electrodes.

A quantitative analysis of the voltage as a function of time (dashed line in Figure 5) is challenging due to the undefined current during the CV phase, as this results in a different ohmic voltage drop that does not correlate with the C-rate in the CC phase. The pseudo equilibrium voltage, which occurs after a sufficiently long relaxation time, depends on the lithiation state of the anode and the cathode, which in turn depends on the capacities reached during the CCCV charging as well as cell ageing and the resulting loss of lithium

inventory. Noteworthy are the differences in pseudo equilibrium voltage after 5C and 3C charging for the cell with an unstructured electrode, in which the measured voltage after 30 min of relaxation is higher after 5C charging (3.94 V) compared to 3C charging (3.92 V). The reason for this may be the similar capacity reached in the CCCV phase, whereby for charging at 3C, a higher amount of lithium plating leads to an overestimated SOC compared to charging at 5C where less additional plating is indicated by less pronounced peaks in the dV/dt for this cell.

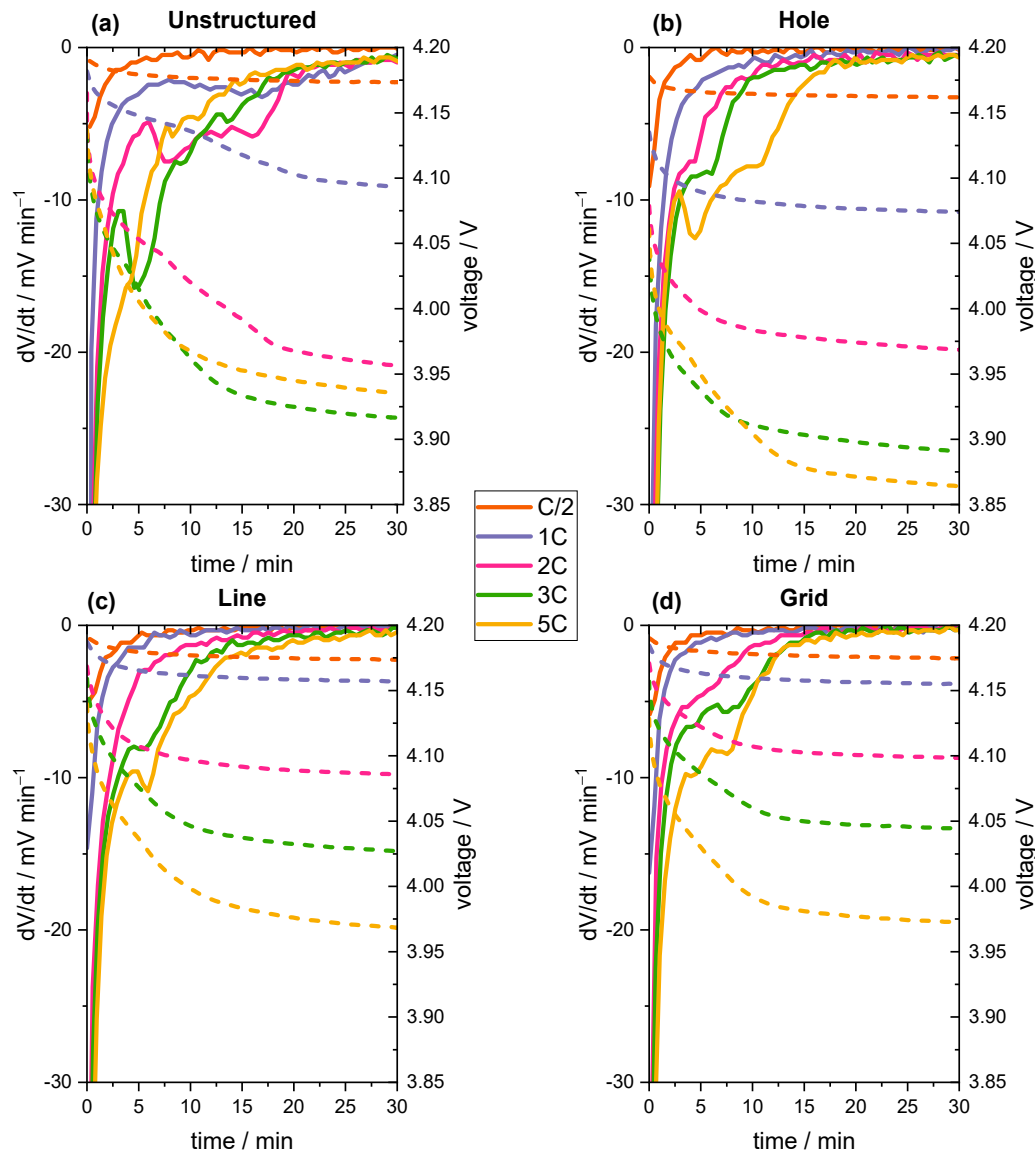


Figure 5. Differential voltage analysis of the voltage relaxation (solid line) and voltage as a function of time (dashed line) in the first 30 min of the 4 h rest period after charging in the fifth cycle at each C-rate for the cells with unstructured (a), hole structured (b), line structured (c), and grid structured (d) electrodes.

3.4. Post-Mortem Analyses

To confirm the results from the dV/dt analyses, the set of cells shown in Figure 5 were disassembled in a fully discharged state after the rate capability test. In Figure 6a–d, optical microscope images of anodes from the unstructured (Figure 6a) and structured cells (Figure 6b–d) are shown. The white round dashed outline in Figure 6a–d indicates the part of the anode surface which was covered by the cathode. As expected from the dV/dt analysis, all cells showed lithium plating on the anode/separators interphase, indicated

by the white-grey colored layer formation [12,30]. The unstructured electrode showed a continuous and dense surface layer formation, while the structured electrodes were only partially covered. As it was not possible to completely avoid a partial stripping of the surface layer during the disassembly process, large parts of the formed surface layer were found on the separator of the unstructured electrode (Figure S2). Whether the visible crack in the center of the electrode with hole structure (Figure 6b,f) is caused by cell disassembly or by cell ageing is not certain. While for the electrode with line and grid structures, large areas of the electrode are recognizable without any surface layer formed, the surface of the electrode with hole structure is covered except for the outermost edge area. All structure types have in common a change in morphology in the form of overgrown structures due to the surface layer that is formed during cell ageing. While overgrown structures are found centered in the electrode with grid structure and in the electrode with line structure, large areas of overgrown structures are found in the edge area (Figure S3) of the electrode with hole structure and only occasionally centered on the electrode (Figure 6f). Similar observations of locally degraded and overgrown electrodes, structured and unstructured, have been found in full-cells in coin and pouch cell format [30,33]. We assume that an overgrowth of the structures and the associated loss of advantage in the diffusion kinetics lead to a decreasing fast-charging performance of the cell. The geometry of the formed surface layer is also noteworthy. All the electrodes analyzed, except for the line-structured electrode, show a spherical geometry of the surface layer formed. The line structured electrode, on the other hand, shows a pattern that is shaped like an ellipse. The distance between the edge of the formed surface layer and the edge of the electrode is therefore almost equidistant. An influence of the wetting and rewetting of the electrode with electrolyte during cycling on the plating behavior is therefore most probable and also explains the higher capacity retention at high C-rates for cells with capillary structures (Figure 3; grid and line).

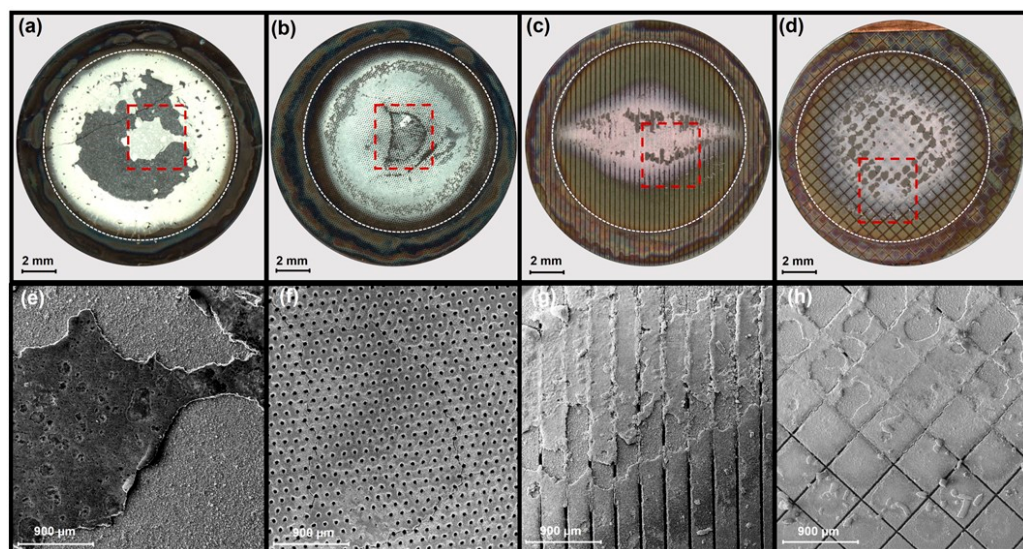


Figure 6. Post-mortem digital microscope images (a–d) and SEM images (e–f) of the unstructured (a,e), hole structured (b,f), line structured (c,g), and grid structured (d,h) electrodes (same set of cells as in Figure 5). White dashed outline marks the anode area which was covered by the cathode and the red dashed outline marks the cut-out of the respective SEM image.

3.5. Extrapolation to Commercial Cell Formats

Coin cells were used in this study because they are easy to manufacture, reproducible, and safe to handle due to their low capacities. However, if one wants to identify the advantages and disadvantages of cells with structured electrodes in terms of the achievable energy and power densities, one must consider commercial cell designs, as the cell design strongly influences the achievable energy density. For this purpose, the energy and power

density were calculated using the geometric data from a commercial pouch cell and the material and electrode characteristics in the work presented [53]. The weight of the packaging material of the cell, i.e., pouch bag and the tapes, is neglected in the calculation. The underlying data for the calculation and the formulae can be found in Equations (S1)–(S18). It should be noted that the stack height is not considered as a limiting factor in this calculation and that the energy density of 674 Wh L^{-1} of the commercial pouch cell in reference [53] (anode areal capacity of 5.23 mAh cm^{-2}) is higher than the data calculated in this work due to the use of optimized electrodes in terms of porosity, active material share, and N/P-ratio. In Figure 7, the calculated specific energy and energy density as a function of the anode areal capacity is shown. The benefits of the implementation of thick-film electrodes can be seen in the increasing energy density and specific energy on cell level with increasing areal capacity. In our calculation, increasing the anode areal capacity from $2 \text{ mAh} \cdot \text{cm}^{-2}$ to $4 \text{ mAh} \cdot \text{cm}^{-2}$ would result in an increase in energy density of 16%. Figure 7 also shows that structuring the anode with a 11% mass loss reduces the achievable energy density at cell level by around 6%. This makes it clear that the comparison of structured electrodes with unstructured electrodes, even if these electrodes have similar areal capacities, puts the unstructured electrodes at a disadvantage when considering large-format cells, as the same energy density could also be achieved with unstructured electrodes with a lower areal capacity. In our case, with an areal capacity of approximately $4.4 \text{ mAh} \cdot \text{cm}^{-2}$ of the structured electrodes and an average mass loss of 11%, the cells with structured electrodes would have to be compared with cells with unstructured electrodes with an areal capacity of $3.15 \text{ mAh} \cdot \text{cm}^{-2}$ (as indicated by the dotted lines and arrows in Figure 7) in order to compare large-format cells with the same energy density later on.

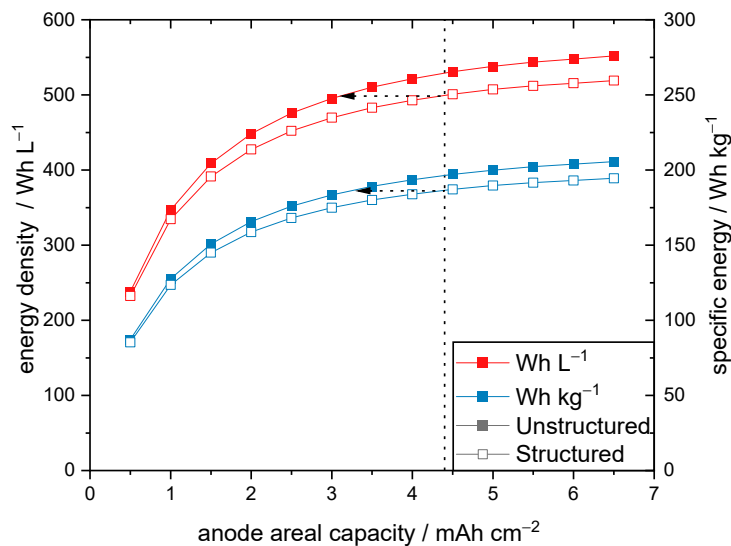


Figure 7. Calculation of the energy density (orange) and specific energy (green) as a function of the anode areal capacity in an 80 Ah pouch cell (cell geometry data extracted from [53]; electrode parameter from this work with an N/P ratio of 1.16) with unstructured (solid symbols) and structured (hollow symbols; 11% mass loss) anodes. The dashed line serves as an aid to orientation for comparing the same energy density or specific energy between cells with structured and unstructured electrodes.

To take this into account, additional reference cells (following referred to as “New Ref.”) were manufactured with an anode surface capacity of $3.2 \text{ mAh} \cdot \text{cm}^{-2}$. However, with an N/P ratio of 1.25, the “New Ref.” full-cells have a higher N/P ratio compared to the cells used in this work, which in turn has a negative effect on the calculated energy density. The production and cell data of the “New Ref.” cells can be found in Figures S4 and S5, and [51]. With the previous investigations on the fast-charging capability and the onset of lithium plating, the minimum charging time to an SOC 80% can now be determined for the analyzed cells. The lowest C-rate, according to which lithium plating was recognized

in the dV/dt , as well as the fastest possible charging times without lithium plating are listed in Table 4. The cells with line structured electrodes showed the highest C-rate for the onset of lithium plating (3C) and thus, the fastest possible charging time without lithium plating at a C-rate of 2C of 24.07 min. This results in a cell with line-structured electrodes being charged 3.6 times faster compared to cells with unstructured electrodes of the same areal capacity.

Table 4. Onset of lithium plating, as determined in dV/dt analysis and minimum charging time up to a SOC of 80% without lithium plating.

	Unstructured	Hole	Line	Grid	New Ref.
dV/dt onset of lithium plating	1C	2C	3C	2C	2C
Charging time to SOC 80%/min	85.57 (C/2)	43.43 (1C)	24.07 (2C)	42.99 (1C)	43.5 (1C)

With the minimum charging times now known, the power density (P_v ; Equation (1)) and specific power (P_m ; Equation (2)) can be calculated in addition to the energy density (E_v) and specific energy (E_m). The equations are as follows:

$$P_v = 0.8 \cdot \frac{E_v}{t_{SOC_{80}}} \quad (1)$$

$$P_m = 0.8 \cdot \frac{E_m}{t_{SOC_{80}}} \quad (2)$$

The resulting power and energy densities as well as the specific power and energy are plotted in Figure 8. Since the information and the tendency of the data regarding specific energy and energy density are highly similar, the further discussion is limited to the energy density. The relatively high N/P ratio of 1.25 of the “New Ref.” cells is the reason for their lower energy density compared to the other cells with an average N/P ratio of 1.16. Comparing the cells with unstructured electrodes, a decrease in areal capacity from 4.3 mAh cm^{-2} to 3.2 mAh cm^{-2} increases the power density by 76% from 299 W L^{-1} to 526 W L^{-1} . All investigated cell types with structured electrodes reached higher calculated power densities than the unstructured reference cells with 3.2 mAh cm^{-2} and 4.3 mAh cm^{-2} . With 987 W L^{-1} , the cell with line structured electrodes has the highest calculated power density of all investigated cell types. Compared to the cell with unstructured electrodes of similar areal capacity (4.3 mAh cm^{-2}), this means an increase in power density of 230% with an energy density that is 6% lower and compared to the “New. Ref.” cells (3.2 mAh cm^{-2}), an increase in power density of 87% with a 4% higher energy density. The high N/P ratio of the “New Ref.” cells (N/P ratio of 1.25) lead to cells with a lower areal capacity of the cathode and thus, to lower current densities at the same C-rate compared to cells with the same anode and lower N/P ratio. This suggests that cells with a areal capacity of 3.2 mAh cm^{-2} and an N/P ratio of 1.16, which would lead to a comparable energy density to the cells with structured electrodes in this work, will have an even lower rate capability and thus, the positive influence on the power density of structured cells with the same N/P ratio and energy density will be even more pronounced.

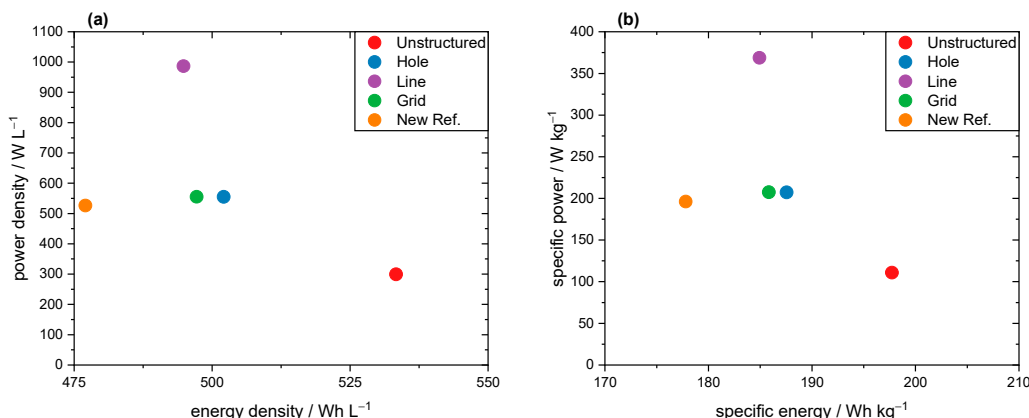


Figure 8. Calculated power and energy data for an 80 Ah pouch cell: (a) volumetric energy and power density; (b) specific energy and power. The geometry data were extracted from [53] and electrode parameters were taken from this work.

4. Conclusions

The fast-charging capability and lithium plating of cells with laser structured anodes of high areal capacity ($>4.3 \text{ mAh cm}^{-2}$) and several structure patterns were investigated in coin cells in full-cell format by dV/dt and post-mortem analysis. Furthermore, EIS measurements in symmetrical cells showed the differences in ionic resistance between structured and unstructured electrodes of similar areal capacity. The resulting energy and power densities of prospective commercial pouch cells with the electrodes used in this work were calculated and potential pitfalls in the comparison to cells with unstructured electrodes were identified. All investigated structure patterns, namely the line, grid, and hole pattern, showed a higher rate capability, lower ionic resistivity, and a lithium plating onset shifting towards higher C-rates, if compared to cells with unstructured anodes of similar areal capacity. The highest fast-charging capability was reached by implementing line structured anodes. The required charging time to a SOC of 80% was reduced by a factor of 3.6 from 85.57 min in the case of cells with unstructured electrodes of similar areal capacity to 24.07 min in the case of cells with line structured anodes and the onset for lithium plating is shifted from charging at 1C to 3C, respectively. In the post-mortem analyses, subsequently to the rate capability test, all cell types, structured and unstructured, showed lithium plating, as expected from the dV/dt analysis, and all structured cells showed parts where the structures were overgrown by the forming surface layer. Noteworthy is the geometry of the formed surface layer formation on the anodes, especially in the case of the cells with line structured electrodes. The distance between the edge of the formed surface layer and the edge of the electrode is therefore almost equidistant along the direction of the line structures. An influence of the wetting and rewetting of the electrode with electrolyte during cycling on the plating behavior is therefore most probable and also explains the lower performance of the cells with hole structures in the rate capability analysis due to the lack of capillary structures. By extrapolating the results from coin cells to commercial pouch cell designs, it was possible to show that attention is required in selecting the reference cell. Due to the laser structuring and the resulting average mass loss of 11% of the anode, the energy density of a commercial pouch cell with these electrodes would decrease about 6% in comparison to cells with unstructured anodes of similar areal capacity. With an areal capacity of approximately 4.4 mAh cm^{-2} of the structured anodes and an average mass loss of 11%, the cells with structured anodes would have to be compared to cells with unstructured electrodes with an areal capacity of 3.15 mAh cm^{-2} in order to compare large-format cells with the same energy density later on. For this reason, new reference cells with anodes with an areal capacity of 3.2 mAh cm^{-2} were manufactured and tested. Comparing the cells with unstructured electrodes, a decrease in areal capacity from 4.3 mAh cm^{-2} to 3.2 mAh cm^{-2} increases the power density by 76% from 399 W L^{-1} to 526 W L^{-1} . All

investigated cell types with structured electrodes reached higher calculated power densities than the unstructured reference cells with 3.2 mAh cm^{-2} and 4.3 mAh cm^{-2} . Cells with line structured electrodes have the highest calculated power density of all investigated cell types. With 987 W L^{-1} , the cells with line structured electrodes have a 230% higher power density and an energy density that is 6% lower compared to cells with unstructured electrodes of similar areal capacity (4.3 mAh cm^{-2}) and compared to the cells with unstructured electrodes of lower areal capacity (3.2 mAh cm^{-2}), an 87% higher power density and a 4% higher energy density due to the differences in the N/P ratio.

Supplementary Materials: The following supporting information can be downloaded at <https://www.mdpi.com/article/10.3390/batteries10050160/s1>, Figure S1: Differential voltage analysis of the voltage relaxation (solid line) and voltage as a function of time (dashed line) in the 4 h rest period after charging in the 5th cycle at each C-rate for all cells with unstructured and structured electrodes; Figure S2: Separator of the cell with unstructured electrodes with plated lithium sticking on it (cathode visible on the backside); Figure S3: Post-mortem digital microscope image of the hole structured electrode with overgrown structures visible in the edge of the plated area, Figure S4: Differential voltage analysis of the voltage relaxation (solid line) and voltage as a function of time (dashed line) in the 4 h rest period after charging in the 5th cycle at each C-rate for the “New Ref.” cells; Figure S5: Specific charge capacity of the “New. Ref.” cells after the CC and CCCV phase (without the 5th cycle at each C-rate). The shading represents the standard deviation, Table S1: Abbreviations and data for calculating the energy density and specific energy, Equations to calculate the energy density and specific energy: Equations (S1)–(S18), Generalized finite Warburg element: Equations (S19)–(S22).

Author Contributions: Conceptualization, Y.S.; methodology, Y.S. and W.P.; validation, Y.S. and W.P.; investigation, Y.S.; resources, W.P.; data curation, Y.S.; writing—original draft preparation, Y.S.; writing—review and editing, W.P.; visualization, Y.S.; supervision, W.P.; project administration, W.P.; funding acquisition, W.P. All authors have read and agreed to the published version of the manuscript.

Funding: This project has received funding from the German Research Foundation (DFG, 3D-Bat-Hybrid, project No. 467624762).

Data Availability Statement: Data are contained within this article and Supplementary Materials.

Acknowledgments: We are grateful to our colleagues U. Rist, M. Kapitz, and A. Reif for their technical and scientific support during electrode manufacturing, laser processing, and scanning electron microscopy.

Conflicts of Interest: The authors declare no conflicts of interest.

References

1. Schmuck, R.; Wagner, R.; Hörpel, G.; Placke, T.; Winter, M. Performance and cost of materials for lithium-based rechargeable automotive batteries. *Nat. Energy* **2018**, *3*, 267–278. [[CrossRef](#)]
2. Weiss, M.; Ruess, R.; Kasnatscheew, J.; Levartovsky, Y.; Levy, N.R.; Minnmann, P.; Stolz, L.; Waldmann, T.; Wohlfahrt-Mehrens, M.; Aurbach, D.; et al. Fast Charging of Lithium-Ion Batteries: A Review of Materials Aspects. *Adv. Energy Mater.* **2021**, *11*, 2101126. [[CrossRef](#)]
3. Link, S.; Neef, C.; Wicke, T. Trends in Automotive Battery Cell Design: A Statistical Analysis of Empirical Data. *Batteries* **2023**, *9*, 261. [[CrossRef](#)]
4. Zhang, N.; Li, J.; Li, H.; Liu, A.; Huang, Q.; Ma, L.; Li, Y.; Dahn, J.R. Structural, Electrochemical, and Thermal Properties of Nickel-Rich $\text{LiNi}_{x}\text{Mn}_{y}\text{Co}_{z}\text{O}_2$ Materials. *Chem. Mater.* **2018**, *30*, 8852–8860. [[CrossRef](#)]
5. Obrovac, M.N.; Chevrier, V.L. Alloy negative electrodes for Li-ion batteries. *Chem. Rev.* **2014**, *114*, 11444–11502. [[CrossRef](#)]
6. Heubner, C.; Nickol, A.; Seeba, J.; Reuber, S.; Junker, N.; Wolter, M.; Schneider, M.; Michaelis, A. Understanding thickness and porosity effects on the electrochemical performance of $\text{LiNi}_{0.6}\text{Co}_{0.2}\text{Mn}_{0.2}\text{O}_2$ -based cathodes for high energy Li-ion batteries. *J. Power Sources* **2019**, *419*, 119–126. [[CrossRef](#)]
7. Gallagher, K.G.; Trask, S.E.; Bauer, C.; Woehrle, T.; Lux, S.F.; Tschech, M.; Lamp, P.; Polzin, B.J.; Ha, S.; Long, B.; et al. Optimizing Areal Capacities through Understanding the Limitations of Lithium-Ion Electrodes. *J. Electrochem. Soc.* **2015**, *163*, A138–A149. [[CrossRef](#)]
8. Heubner, C.; Schneider, M.; Michaelis, A. Diffusion-Limited C-Rate: A Fundamental Principle Quantifying the Intrinsic Limits of Li-Ion Batteries. *Adv. Energy Mater.* **2019**, *10*, 1902523. [[CrossRef](#)]

9. Colclasure, A.M.; Dunlop, A.R.; Trask, S.E.; Polzin, B.J.; Jansen, A.N.; Smith, K. Requirements for Enabling Extreme Fast Charging of High Energy Density Li-Ion Cells while Avoiding Lithium Plating. *J. Electrochem. Soc.* **2019**, *166*, A1412–A1424. [[CrossRef](#)]
10. Uhlmann, C.; Illig, J.; Ender, M.; Schuster, R.; Ivers-Tiffée, E. In situ detection of lithium metal plating on graphite in experimental cells. *J. Power Sources* **2015**, *279*, 428–438. [[CrossRef](#)]
11. Waldmann, T.; Hogg, B.-I.; Wohlfahrt-Mehrens, M. Li plating as unwanted side reaction in commercial Li-ion cells—A review. *J. Power Sources* **2018**, *384*, 107–124. [[CrossRef](#)]
12. Chen, Y.; Chen, K.-H.; Sanchez, A.J.; Kazyak, E.; Goel, V.; Gorlin, Y.; Christensen, J.; Thornton, K.; Dasgupta, N.P. Operando video microscopy of Li plating and re-intercalation on graphite anodes during fast charging. *J. Mater. Chem. A* **2021**, *9*, 23522–23536. [[CrossRef](#)]
13. Petzl, M.; Kasper, M.; Danzer, M.A. Lithium plating in a commercial lithium-ion battery—A low-temperature aging study. *J. Power Sources* **2015**, *275*, 799–807. [[CrossRef](#)]
14. Konz, Z.M.; McShane, E.J.; McCloskey, B.D. Detecting the Onset of Lithium Plating and Monitoring Fast Charging Performance with Voltage Relaxation. *ACS Energy Lett.* **2020**, *5*, 1750–1757. [[CrossRef](#)]
15. Chen, K.H.; Goel, V.; Namkoong, M.J.; Wied, M.; Müller, S.; Wood, V.; Sakamoto, J.; Thornton, K.; Dasgupta, N.P. Enabling 6C Fast Charging of Li-Ion Batteries with Graphite/Hard Carbon Hybrid Anodes. *Adv. Energy Mater.* **2020**, *11*, 2003336. [[CrossRef](#)]
16. Gottschalk, L.; Strzelczyk, N.; Adam, A.; Kwade, A. Influence of different anode active materials and blends on the performance and fast-charging capability of lithium-ion battery cells. *J. Energy Storage* **2023**, *68*, 107706. [[CrossRef](#)]
17. Strzelczyk, N.; Gottschalk, L.; Müller, J.; Kwade, A. The Influence of Calendering on the Fast Charging Performance and Lithium Plating of Hard Carbon Blend Anodes. *Energy Technol.* **2022**, *11*, 2200865. [[CrossRef](#)]
18. Gottschalk, L.; Oertel, C.; Strzelczyk, N.; Müller, J.; Krüger, J.; Haselrieder, W.; Kwade, A. Improving the Performance of Lithium-Ion Batteries Using a Two-Layer, Hard Carbon-Containing Silicon Anode for Use in High-Energy Electrodes. *Energy Technol.* **2022**, *11*, 2200858. [[CrossRef](#)]
19. Gottschalk, L.; Müller, J.; Schoo, A.; Baasch, E.; Kwade, A. Spherical Graphite Anodes: Influence of Particle Size Distribution and Multilayer Structuring in Lithium-Ion Battery Cells. *Batteries* **2024**, *10*, 40. [[CrossRef](#)]
20. Müller, D.; Fill, A.; Birke, K.P. Cycling of Double-Layered Graphite Anodes in Pouch-Cells. *Batteries* **2022**, *8*, 22. [[CrossRef](#)]
21. Müller, D.; Landa-Medrano, I.; Eguia-Barrio, A.; Boyano, I.; Urdampilleta, I.; de Meatza, I.; Fill, A.; Birke, P. Electrochemical characterization of bi-layered graphite anodes combining high and low porosity in lithium-ion cells to improve cell performance. *Electrochim. Acta* **2021**, *391*, 138966. [[CrossRef](#)]
22. Pfleging, W. Recent progress in laser texturing of battery materials: A review of tuning electrochemical performances, related material development, and prospects for large-scale manufacturing. *Int. J. Extrem. Manuf.* **2020**, *3*, 012002. [[CrossRef](#)]
23. Keilhofer, J.; Schaffranka, L.W.F.; Wuttke, A.; Günter, F.J.; Hille, L.; Dorau, F.A.; Daub, R. Mechanical Structuring of Lithium-Ion Battery Electrodes Using an Embossing Roller. *Energy Technol.* **2023**, *11*, 2200869. [[CrossRef](#)]
24. Delattre, B.; Amin, R.; Sander, J.; De Coninck, J.; Tomsia, A.P.; Chiang, Y.-M. Impact of Pore Tortuosity on Electrode Kinetics in Lithium Battery Electrodes: Study in Directionally Freeze-Cast LiNi_{0.8}Co_{0.15}Al_{0.05}O₂(NCA). *J. Electrochem. Soc.* **2018**, *165*, A388–A395. [[CrossRef](#)]
25. Rist, U.; Falkowski, V.; Pfleging, W. Electrochemical Properties of Laser-Printed Multilayer Anodes for Lithium-Ion Batteries. *Nanomaterials* **2023**, *13*, 2411. [[CrossRef](#)]
26. Shi, C.; Yu, M. Flexible solid-state lithium-sulfur batteries based on structural designs. *Energy Storage Mater.* **2023**, *57*, 429–459. [[CrossRef](#)]
27. Hille, L.; Noecker, M.P.; Ko, B.; Kriegler, J.; Keilhofer, J.; Stock, S.; Zaeh, M.F. Integration of laser structuring into the electrode manufacturing process chain for lithium-ion batteries. *J. Power Sources* **2023**, *556*, 232478. [[CrossRef](#)]
28. Meyer, A.; Zhu, P.; Smith, A.; Pfleging, W. Gaining a New Technological Readiness Level for Laser-Structured Electrodes in High-Capacity Lithium-Ion Pouch Cells. *Batteries* **2023**, *9*, 548. [[CrossRef](#)]
29. Hille, L.; Kriegler, J.; Oehler, A.; Chaja, M.; Wagner, S.; Zaeh, M.F. Picosecond laser structuring of graphite anodes—Ablation characteristics and process scaling. *J. Laser Appl.* **2023**, *35*, 042054. [[CrossRef](#)]
30. Kriegler, J.; Hille, L.; Stock, S.; Kraft, L.; Hagemeister, J.; Habedank, J.B.; Jossen, A.; Zaeh, M.F. Enhanced performance and lifetime of lithium-ion batteries by laser structuring of graphite anodes. *Appl. Energy* **2021**, *303*, 117693. [[CrossRef](#)]
31. Chen, K.-H.; Namkoong, M.J.; Goel, V.; Yang, C.; Kazemiabnavi, S.; Mortuza, S.M.; Kazyak, E.; Mazumder, J.; Thornton, K.; Sakamoto, J.; et al. Efficient fast-charging of lithium-ion batteries enabled by laser-patterned three-dimensional graphite anode architectures. *J. Power Sources* **2020**, *471*, 228475. [[CrossRef](#)]
32. Habedank, J.B.; Kriegler, J.; Zaeh, M.F. Enhanced Fast Charging and Reduced Lithium-Plating by Laser-Structured Anodes for Lithium-Ion Batteries. *J. Electrochem. Soc.* **2019**, *166*, A3940–A3949. [[CrossRef](#)]
33. Dunlap, N.; Sulas-Kern, D.B.; Weddle, P.J.; Usseglio-Viretta, F.; Walker, P.; Todd, P.; Boone, D.; Colclasure, A.M.; Smith, K.; Tremolet de Villers, B.J.; et al. Laser ablation for structuring Li-ion electrodes for fast charging and its impact on material properties, rate capability, Li plating, and wetting. *J. Power Sources* **2022**, *537*, 231464. [[CrossRef](#)]
34. Dubey, R.; Zwahlen, M.D.; Shynkarenko, Y.; Yakunin, S.; Fuerst, A.; Kovalenko, M.V.; Kravchyk, K.V. Laser Patterning of High-Mass-Loading Graphite Anodes for High-Performance Li-Ion Batteries. *Batter. Supercaps* **2020**, *4*, 464–468. [[CrossRef](#)]
35. Park, J.; Jeon, C.; Kim, W.; Bong, S.-J.; Jeong, S.; Kim, H.-J. Challenges, laser processing and electrochemical characteristics on application of ultra-thick electrode for high-energy lithium-ion battery. *J. Power Sources* **2021**, *482*, 228948. [[CrossRef](#)]

36. Schweighofer, L.; Eschelmuller, B.; Frohlich, K.; Pfleging, W.; Pichler, F. Modelling and Optimisation of Laser-Structured Battery Electrodes. *Nanomaterials* **2022**, *12*, 1574. [CrossRef] [PubMed]
37. Zheng, Y.; Seifert, H.J.; Shi, H.; Zhang, Y.; Kübel, C.; Pfleging, W. 3D silicon/graphite composite electrodes for high-energy lithium-ion batteries. *Electrochim. Acta* **2019**, *317*, 502–508. [CrossRef]
38. Meyer, A.; Ball, F.; Pfleging, W. The Effect of Silicon Grade and Electrode Architecture on the Performance of Advanced Anodes for Next Generation Lithium-Ion Cells. *Nanomaterials* **2021**, *11*, 3448. [CrossRef] [PubMed]
39. Zhu, P.; Ebert, B.; Smyrek, P.; Pfleging, W. The Impact of Structural Pattern Types on the Electrochemical Performance of Ultra-Thick NMC 622 Electrodes for Lithium-Ion Batteries. *Batteries* **2024**, *10*, 58. [CrossRef]
40. Kumberg, J.; Müller, M.; Diehm, R.; Spiegel, S.; Wachsmann, C.; Bauer, W.; Scharfer, P.; Schabel, W. Drying of Lithium-Ion Battery Anodes for Use in High-Energy Cells: Influence of Electrode Thickness on Drying Time, Adhesion, and Crack Formation. *Energy Technology* **2019**, *7*, 1900722. [CrossRef]
41. Meyer, A.; Sterzl, Y.; Pfleging, W. High repetition ultrafast laser ablation of graphite and silicon/graphite composite electrodes for lithium-ion batteries. *J. Laser Appl.* **2023**, *35*, 042036. [CrossRef]
42. Kouli, M.; Kandula, M.W.; Dilger, K.; Klotzbach, U.; Kling, R.; Watanabe, A. Laser-material-interactions between ultrashort pulse lasers and electrodes for lithium-ion batteries during micro-structuring the electrode surface. In Proceedings of the Laser-Based Micro- and Nanoprocessing XV, San Francisco, CA, USA, 27 October 2021; SPIE: Bellingham, WA, USA, 2021.
43. Landesfeind, J.; Hattendorff, J.; Ehrl, A.; Wall, W.A.; Gasteiger, H.A. Tortuosity Determination of Battery Electrodes and Separators by Impedance Spectroscopy. *J. Electrochem. Soc.* **2016**, *163*, A1373–A1387. [CrossRef]
44. Ogihara, N.; Itou, Y.; Sasaki, T.; Takeuchi, Y. Impedance Spectroscopy Characterization of Porous Electrodes under Different Electrode Thickness Using a Symmetric Cell for High-Performance Lithium-Ion Batteries. *J. Phys. Chem. C* **2015**, *119*, 4612–4619. [CrossRef]
45. Nguyen, T.-T.; Demortière, A.; Fleutot, B.; Delobel, B.; Delacourt, C.; Cooper, S.J. The electrode tortuosity factor: Why the conventional tortuosity factor is not well suited for quantifying transport in porous Li-ion battery electrodes and what to use instead. *Npj Comput. Mater.* **2020**, *6*, 123. [CrossRef]
46. Lasia, A. Modeling of Impedance of Porous Electrodes. In *Modeling and Numerical Simulations I*; Springer: New York, NY, USA, 2009; pp. 67–137.
47. Schneider, L.; Klemens, J.; Herbst, E.C.; Müller, M.; Scharfer, P.; Schabel, W.; Bauer, W.; Ehrenberg, H. Transport Properties in Electrodes for Lithium-Ion Batteries: Comparison of Compact versus Porous NCM Particles. *J. Electrochem. Soc.* **2022**, *169*, 100553. [CrossRef]
48. De Lauri, V.; Krumbein, L.; Hein, S.; Prifling, B.; Schmidt, V.; Danner, T.; Latz, A. Beneficial Effects of Three-Dimensional Structured Electrodes for the Fast Charging of Lithium-Ion Batteries. *ACS Appl. Energy Mater.* **2021**, *4*, 13847–13859. [CrossRef]
49. Pfleging, W.; Pröll, J. A new approach for rapid electrolyte wetting in tape cast electrodes for lithium-ion batteries. *J. Mater. Chem. A* **2014**, *2*, 14918–14926. [CrossRef]
50. Habedank, J.B.; Günter, F.J.; Billot, N.; Gilles, R.; Neuwirth, T.; Reinhart, G.; Zaeh, M.F. Rapid electrolyte wetting of lithium-ion batteries containing laser structured electrodes: In situ visualization by neutron radiography. *Int. J. Adv. Manuf. Technol.* **2019**, *102*, 2769–2778. [CrossRef]
51. Sterzl, Y.; Pfleging, W.; Kling, R.; Pfleging, W.; Sugioka, K. An electrode design study: Laser structuring of anodes for fast-charging of batteries. In Proceedings of the Laser-Based Micro- and Nanoprocessing XVIII, San Francisco, CA, USA, 27 January–1 February 2024; SPIE: Bellingham, WA, USA, 2024.
52. Von Lüders, C.; Zinth, V.; Erhard, S.V.; Osswald, P.J.; Hofmann, M.; Gilles, R.; Jossen, A. Lithium plating in lithium-ion batteries investigated by voltage relaxation and in situ neutron diffraction. *J. Power Sources* **2017**, *342*, 17–23. [CrossRef]
53. Günter, F.J.; Wassiliadis, N. State of the Art of Lithium-Ion Pouch Cells in Automotive Applications: Cell Teardown and Characterization. *J. Electrochem. Soc.* **2022**, *169*, 030515. [CrossRef]

Disclaimer/Publisher’s Note: The statements, opinions and data contained in all publications are solely those of the individual author(s) and contributor(s) and not of MDPI and/or the editor(s). MDPI and/or the editor(s) disclaim responsibility for any injury to people or property resulting from any ideas, methods, instructions or products referred to in the content.